JOURNAL OF PROPULSION AND POWER
Vol. 12, No. 5, September–October 1996

# Numerical Simulation of Dynamic Wave Rotor Performance

Daniel E. Paxson*
*NASA Lewis Research Center, Cleveland, Ohio 44135*

**A numerical model has been developed that can simulate the dynamic (and steady-state) performance of a wave rotor, given the geometry and time-dependent boundary conditions. The one-dimensional, perfect-gas, computational fluid dynamics-based code tracks the gasdynamics in each of the wave rotor passages as they rotate past the various ducts. The model can operate both on and off-design, allowing dynamic behavior to be studied throughout the operating range of the wave rotor. The model accounts for several major loss mechanisms including finite passage opening time, fluid friction, heat transfer to and from the passage walls, and leakage to and from the passage ends. In addition it can calculate the amount of work transferred to or from the fluid when the flow in the ducts is not aligned with the passages such as occurs in off-design operation. Since it is one-dimensional, the model runs reasonably fast on a typical workstation. This article will describe the model and present the results of some transient calculations for a conceptual four-port wave rotor designed as a topping cycle for a small gas-turbine engine.**

## Nomenclature

$A$ = cross-sectional area
$[A]$ = flux Jacobian
$a$ = speed of sound
$b$ = passage width
$b_{ci}$ = circumferential span of the combustor inlet port
$C_D$ = leakage gap discharge coefficient, assumed to be 0.8
$c$ = specific heat
$D_h$ = passage hydraulic diameter
$\underline{F}$ = normalized flux vector
$\underline{f}$ = numerical flux vector estimate
$g_c$ = Newton constant
$h$ = passage height
$k$ = passage index
$L$ = passage length
$M$ = last computational cell in the computing domain
$\dot{m}$ = mass flow rate
$N$ = number of passages
$P$ = normalized stagnation pressure
$P'$ = stagnation pressure
$Pr$ = Prandtl number
$p'$ = static pressure
$p$ = normalized static pressure
$\underline{Q}$ = heat addition rate
$R$ = rotor mean radius
$R_g$ = real gas constant
$Re$ = Reynolds number, $\rho' aL/\mu$
$\underline{S}$ = normalized source term vector
$\underline{s}$ = numerical source term vector estimate
$s_1, s_2, s_3$ = components of $\underline{S}$
$T$ = normalized static temperature
$T'$ = stagnation temperature
$T^0$ = normalized stagnation temperature
$t$ = normalized time, time divided by $L/a^*$
$u$ = normalized velocity
$V$ = volume
$\underline{w}$ = normalized conserved fluid state vector
$x$ = normalized axial position (distance divided by rotor length)
$\gamma$ = ratio of specific heats
$\gamma_2$ = $\sqrt{2/(\gamma - 1)}$
$\Delta$ = numerical spacing
$\delta_{leak}$ = leakage gap between rotor end and casing (assumed $\ll \Delta x$)
$\zeta_{cl}$ = combustor cold pressure loss coefficient
$\mu$ = dynamic viscosity
$\rho'$ = density
$\rho$ = normalized density
$\sigma_2$ = source term friction factor coefficient
$\phi$ = product of Biot and Fourier moduli
$\omega$ = rotor angular speed

*Subscripts*
$c$ = corrected
cav = cavity or space located inside the wave rotor housing that is not occupied by rotor material
ci = combustor inlet
co = combustor outlet
com = combustor
$i$ = numerical spacial index
in = inlet
leak = region of passage where leakage occurs

*Superscripts*
$n$ = numerical temporal index
int = intermediate region of rotor passage (between assumed leakage regions)
$*$ = reference quantity for normalization

Presented as Paper 95-2800 at the AIAA/SAE/ASME/ASEE 31st Joint Propulsion Conference, San Diego, CA, July 10–12, 1995; received Oct. 13, 1995; revision received April 27, 1996; accepted for publication May 7, 1996. 

*Aerospace Engineer, Controls and Dynamics Technology Branch, M/S 77-1. Member AIAA.

## Introduction

THE wave rotor is being investigated for use as a core gas generator in future multispool gas-turbine engines to achieve high peak cycle temperatures and pressures with conventional materials technology. The device, shown schematically in Fig. 1, uses gasdynamic waves to transfer energy directly to and from the working fluid through which the waves travel. Many descriptions of wave rotor operating principles

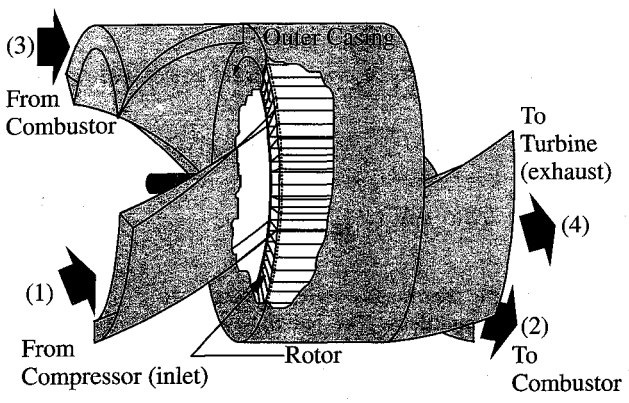


**Fig. 1 Schematic of a four-port wave rotor.**

exist in the literature (Ref. 1 contains citations for several), and to save space one will not be provided here.

The wave rotor is inherently an unsteady device in that gasdynamic waves are continually traversing the passages as they rotate within the casing; however, aside from the periodic fluctuations arising from the opening and closing of the passages as they enter and exit port regions, the flows in the ports are steady as long as the external boundary conditions are constant in time. This condition shall be referred to as steady-state operation. Referring to Fig. 1, the external boundaries include the combustor fuel flow rate, the upstream compressor discharge state, the downstream turbine inlet state, the rotor speed, and in this model, the rotor housing that is assumed adiabatic.

Although the steady-state performance of the wave rotor appears promising for topping conventional gas-turbine engines,[2-4] critical questions concerning transient and dynamic performance remain. For example, how does the wave rotor respond to fuel flow changes? Does a wave rotor exhibit instabilities such as surge? How does transient behavior compare with that of conventional turbomachinery? To answer these and other questions, a numerical model has been developed that simulates the dynamic state of the fluid in all of the passages of the wave rotor as they are exposed to time-dependent conditions in the various ports. The passages are assumed to have uniform properties at any cross section (i.e., one-dimensional flow), and the gas is assumed calorically and thermally perfect. Besides simulating the unsteady gasdynamics that govern the wave rotor operation, the model also simulates losses associated with viscosity, heat transfer to and from the passage walls, the finite opening time of the passages as they enter and exit port regions, nonuniformities in the port flows, and gas leakage between the passage ends and the stationary walls to and from the cavity in the center of the rotor.[5-7] It is also capable of calculating the off-design work transfer that occurs when the flow in the ducts is not aligned with the rotor passages (i.e., flow turning). Since all of the passages are tracked simultaneously it is also possible to calculate the instantaneous torque on the drive shaft and, if no drive motor is present, the acceleration of the rotor shaft. The combustor, the cavity in the center of the wave rotor, and the rotor wall metal have much longer response times than the gasdynamic waves in the rotor passages and have been modeled using lumped volume techniques. To the author's knowledge, this model represents the first transient wave rotor simulation in the literature.

This article will describe the model. Results from several example simulations will be then presented and discussed, followed by some closing remarks.

## Model Description

Much of the passage gasdynamic modeling has been described in other references.[1,5-7] In these papers only a single passage of the wave rotor was followed as it rotated about the circumference; however, the approach to the internal flow is exactly the same in the present multipassage model. As such, equations will be repeated here for reference, but will not be discussed.

### Governing Equations

The governing equations in the passages are assumed to have the following nondimensional form:

$$\frac{\partial \underline{w}}{\partial t} + \frac{\partial \underline{F}(\underline{w})}{\partial x} = \underline{S}(\underline{w}) \tag{1}$$

where

$$\underline{w} = \begin{bmatrix} \rho \\ \rho u \\ \left(\dfrac{p}{\gamma(\gamma-1)} + \dfrac{\rho u^2}{2}\right) \end{bmatrix} \tag{2}$$

$$\underline{F} = \begin{bmatrix} \rho u \\ \dfrac{p}{\gamma} + \rho u^2 \\ u\left(\dfrac{p}{(\gamma-1)} + \dfrac{\rho u^2}{2}\right) \end{bmatrix} \tag{3}$$

together with the perfect gas law that may be written as $p = \rho T$. For the results to be presented, the reference state by which the equations are nondimensionalized is presented in Table 1. The source vector $\underline{S}(\underline{w})$ accounts for viscous effects (i.e., friction), heat transfer from the passage walls to the gas, and leakage from the passages to the hollow center cavity of the rotor and to the ports. Leakage is assumed to occur only at the ends of any passage. Thus, for the intermediate region where there is no leakage the source vector may be written as

$$\underline{S}^{\text{int}} = \begin{bmatrix} 0 \\ \sigma_2 |\rho u|^{0.75} u \\ \dfrac{\sigma_2}{\gamma - 1}\left(\dfrac{D_h}{2h}\right) Pr^{-2/3}(T - T_{\text{wall}})|\rho u|^{0.75} \end{bmatrix} \tag{4}$$

The term $\sigma_2$ is a semiempirically derived constant[7] based on the passage geometry and reference conditions:

$$\sigma_2 = -13.73(L/D_h)^{1.267}(Re^*)^{-0.4935} \tag{5}$$

The dynamic viscosity is assumed constant. The third term of the source vector in Eq. (4) is derived from the Reynolds–Colburn heat transfer, skin friction analogy[8] with heat transfer assumed to occur only from the upper and lower surfaces of the passage, not from the sides.

**Table 1 Wave rotor dimensions and design performance**

| |
|---|
| Mean rotor radius, 8.15 cm (3.2 in.) |
| Rotor length, 15.24 cm (6.0 in.) |
| Rotor passage height, 2.24 cm (0.88 in.) |
| Rotational speed, 16,800 rpm |
| Cycles/revolution, 2 |
| Number of passages, 52 |
| Mass flow rate, 2.3 kg/s (5.0 lbm/s) |
| $P_4/P_1$ (Figs. 1 or 2), 1.22 |
| $T_4/T_1$, 2.21 |
| $T'_{\text{in}}$, 600.9 K (1081.7°R) |
| $p^*$ (also $P_{\text{in}}$), 787.2 kPa (114.2 psia) |
| $\rho^*$, 4.55 kg/m$^3$ (0.284 lbm/ft$^3$) |
| $a^*$, 478.8 m/s (1600.5 ft/s) |

For the ends of the passage where leakage occurs, the source vector is written as

$$\underline{S}^{\text{leak}} = \underline{S}^{\text{int}} + \begin{bmatrix} -C_D\gamma_2\left(\frac{2\delta_{\text{leak}}}{h\Delta x}\right)\sqrt{p\rho}f\left(\frac{P_{\text{cav}}}{p}\right) \\ 0 \\ -C_D\frac{\gamma_2}{(\gamma-1)}\left(\frac{2\delta_{\text{leak}}}{h\Delta x}\right)T^0\sqrt{p\rho}f\left(\frac{P_{\text{cav}}}{p}\right) \end{bmatrix} \tag{6}$$

where the function $f(p_{\text{cav}}/p)$ is the well-known St. Venant's orifice equation.[9] If the cavity pressure is greater than cell pressure, then the pressure ratio in Eq. (6) is inverted, the sign changes, and $p$, $\rho$, and $T^0$ become those of the rotor center cavity.

Equation (1) is integrated numerically using the following Lax–Wendroff technique[1]:

$$\underline{w}_i^{n+1} = \underline{w}_i^n - (\underline{f}_{i+1/2}^n - \underline{f}_{i-1/2}^n)\frac{\Delta t}{\Delta x} + \underline{s}_i^n\Delta t \tag{7}$$

where

$$\underline{f}_{i+1/2}^n = \frac{\underline{\underline{F}}_{i+1}^n + \underline{\underline{F}}_i^n}{2} - \frac{\underline{\underline{\Phi}}_{i+1/2}^{\text{Roe}}}{2} + \frac{\Delta t}{4}([A]_{i+1}^n\underline{S}_{i+1}^n + [A]_i^n\underline{S}_i^n) \tag{8}$$

$$\underline{s}_i^n = \tfrac{1}{2}(3\underline{S}_i^n - \underline{S}_i^{n-1}) \tag{9}$$

The term $\underline{\underline{\Phi}}^{\text{Roe}}$ in Eq. (8) refers to the flux-limited dissipation based on Roe's[10] approximate Riemann solver for Eq. (1) without a source vector. This integration scheme is formally second-order accurate in regions where the flow is smooth, and maintains the high resolution of Roe's method in the vicinity of shocks and density discontinuities. Unless otherwise stated, all results to be presented in this article used a ratio of $\Delta t/\Delta x = 0.3$, with $\Delta x = 0.02$. This grid spacing represents a compromise by the author between the numerical accuracy and the time (i.e., computing resources) required for computing a transient simulation. As such, the choice was necessarily subjective, but this does not detract from the results to be presented. It should be noted that the term numerical accuracy raises difficulties for hyperbolic equations when integrated with Lax–Wendroff based schemes, such as the one used here. Without regard to roundoff error, these schemes become increasingly accurate with decreasing time step in smooth regions of the flow. In regions with discontinuities, however, small time steps result in an artificial spacial diffusion of shock waves and density discontinuities that are implicit in wave rotors. Since the accurate capturing of these discontinuities is critical to modeling wave rotor behavior, the largest possible time step with which numerical stability may be maintained throughout a cycle has been used for these simulations. In steady-state simulations[1,7] this approach has yielded the best match with experimental data. The leakage source term, Eq. (6), is applied to the first and last cell in the computing domain.

### Passage Wall Temperature

The wall temperature for each computational cell of each passage is updated using simple Euler integration on a lumped-capacitance model of the wall section via

$$T_{\text{wall}_i}^{n+1} = T_{\text{wall}_i}^n + [-\phi_1(s_3^{\text{int}})_i^n + \phi_2(T_{\text{cav}}^n - T_{\text{wall}_i}^n)]\Delta t$$

$$\phi_1 = \frac{\gamma-1}{2}\left(\frac{h}{\delta_{\text{wall}}}\right)\left(\frac{1}{\rho_{\text{wall}}}\right)\left(\frac{c_p}{c_{\text{wall}}}\right) \tag{10}$$

$$\phi_2 = \frac{0.04}{\gamma-1}Pr^{-0.4}Re^{*-0.2}\phi_1\left(\frac{L}{h}\right)\left(\frac{R}{L}\right)^{0.6}\left(\frac{\rho_{\text{cav}}^n\omega L}{a^*}\right)^{0.8}$$

where the coefficient $\phi_2$ is the product of the Fourier and Biot moduli[8] for the outer surface of the wall. The heat transfer coefficient in $\phi_2$ was derived from a correlation for steady turbulent flow over a flat plate[11] with the flat plate length replaced by the rotor circumference. Use of a crude integration scheme in Eq. (10) while using a time-accurate scheme for Eq. (7) is justified since the time constants associated with transients in the wall temperature (and those of the gas in the center cavity and combustor to be discussed later) are much larger than the passage wave transit time or even the time for one complete wave cycle.

### Center Cavity

The gas state in the rotor center cavity is also integrated using a simple lumped-capacitance technique. Changes in the gas state arise because of the heat transferred from the rotor inner and outer wall surfaces and because of leakage from the passage ends. The cavity density and pressure may be integrated using continuity and energy equations written in the following form:

$$\rho_{\text{cav}}^{n+1} = \rho_{\text{cav}}^n - \left(\frac{bhL}{V_{\text{cav}}}\right)\sum_{k=1}^{N}([s_1^{\text{leak}}]_{i=1,k}^n + [s_1^{\text{leak}}]_{i=M,k}^n)\Delta x\Delta t$$

$$P_{\text{cav}}^{n+1} = P_{\text{cav}}^n - \left(\frac{bhL}{V_{\text{cav}}}\right)\sum_{k=1}^{N}\left\{(\gamma-1)([s_3^{\text{leak}}]_{i=1,k}^n + [s_3^{\text{leak}}]_{i=M,k}^n) - \phi_3\sum_{i=1}^{M}(T_{\text{wall}_i}^n - T_{\text{cav}}^n)\right\}\Delta x\Delta t \tag{11}$$

$$\phi_3 = 0.04\gamma Pr^{-0.4}Re^{*-0.2}\left(\frac{L}{h}\right)\left(\frac{R}{L}\right)^{0.6}\left(\frac{\rho_{\text{cav}}^n\omega L}{a^*}\right)^{0.8}$$

The wave rotor casing is assumed adiabatic. The gas in the center cavity is assumed to have negligible kinetic energy.

### Combustor

The combustor density and pressure are modeled similarly to the center cavity, except that there is an allowance for heat addition in the energy equation, i.e.,

$$\rho_{\text{com}}^{n+1} = \rho_{\text{com}}^n - \left(\frac{bhL}{V_{\text{com}}}\right)\left\{\sum_{k=1}^{N_{\text{co}}}[F_1]_{i=0,k}^n - \sum_{k=1}^{N_{\text{ci}}}[F_1]_{i=M+1,k}^n\right\}\Delta t$$

$$P_{\text{com}}^{n+1} = P_{\text{com}}^n - \left\{\left(\frac{bhL}{V_{\text{com}}}\right)\gamma\left(T_{\text{com}}^n\sum_{k=1}^{N_{\text{co}}}[F_1]_{i=0,k}^n - T_{\text{ci}}^n\sum_{k=1}^{N_{\text{ci}}}[F_1]_{i=M+1,k}^n\right) - \frac{(\gamma-1)QL}{V_{\text{com}}p^*a^*}\right\}\Delta t \tag{12}$$

where

$$T_{\text{ci}}^n = \frac{\sum_{k=1}^{N_{\text{ci}}}[F_3]_{i=M,k}^n}{\sum_{k=1}^{N_{\text{ci}}}[F_1]_{i=M,k}^n} + \frac{\gamma-1}{2}\left(\frac{\omega R}{a^*}\right)^2 \tag{13}$$

Referring to Fig. 1, the integers $N_{\text{co}}$ and $N_{\text{ci}}$ indicate summations over those passages that are exposed (or partially exposed in the case of finite opening time) to the combustor outlet port and combustor inlet port, respectively.

The combustor state obtained from Eq. (12) is used to update the inlet stagnation conditions for those rotor passages that are exposed to the combustor outlet port at the next time step (i.e., inflow boundary conditions, see Refs. 5 and 7). The passages exposed to the combustor inlet port (i.e., outflow boundary conditions) require an updated static pressure. This is obtained by first estimating the stagnation pressure for the

gas just upstream of the combustor using the following equation:

$$P_{ci}^{n+1} = P_{com}^{n+1} + \frac{\gamma}{2\bar{\rho}_{ci}}\left(\frac{b}{N_{ci}b_{ci}}\sum_{k=1}^{N_{ci}}[F_1]_{i=M+1,k}^{n}\right)^2\left\{\zeta_{cl} - \frac{T_{ci}^{n}}{T_{com}^{n+1}}\right\} \tag{14}$$

where $\bar{\rho}_{ci}$ is the mixed absolute static density of the combustor inlet port flow,[12] and $\zeta_{cl}$ is a constant value greater than 1 that provides a so-called cold pressure loss in addition to that which is incurred by simply heating the gas at constant velocity and static pressure as is assumed in this combustor model. The value of $\zeta_{cl}$ used here is 2.05 which, though ultimately provided by ducting and the combustor liner, is determined by the balanced design point wave diagram.[3] With the combustor inlet stagnation pressure known, the estimated rotor face static pressure required by the model is obtained using the following steady isentropic relation:

$$p_{ci}^{n+1} = P_{ci}^{n+1}(\bar{p}_{ci}^{n}/\bar{\rho}_{ci}^{n}T_{ci}^{n})^{\gamma/(\gamma-1)} \tag{15}$$

where $\bar{p}_{ci}$ is the mixed relative static pressure of the combustor inlet port flow.[12]

#### Boundary Conditions

Implementation of boundary conditions in the model is discussed in detail in Refs. 5–7 and will not be presented here. Suffice it to say that the boundary condition routines contain submodels that account for the effects of finite opening time as each passage enters and exits a port region, and flow turning when the nominally steady flow in the port is not aligned with the flow in the wave rotor passages. Furthermore, they allow computations to continue in extreme off-design situations where portions of the port flows may be reversed from their intended directions. The torque on the rotor may be calculated at any instant of time by summing the product of mass flow rate and the change in tangential velocity from the duct to the adjacent computational cell over all the passages with inflow.

## Example Wave Rotor Description and Steady-State Behavior

The wave rotor chosen for this article has been designed as a four-port topping cycle for a 2.3-kg/s (5-lbm/s) engine, with an upstream compressor pressure ratio of approximately 8. The design technique used is described in Ref. 4. Table 1 shows the relevant dimensions and design point performance. Figure 2 illustrates the design point wave pattern using contours of density plotted as a function of circumferential and axial distance. This may be thought of as a time-averaged view (averaged over the time required for a passage to open) of the standing wave pattern that a stationary observer would see. Although not directly related to dynamic performance, it is interesting to note that the flow going to the combustor (port 2) is a mixture of both compressed fresh air from the inlet (port 1) and hot gas that did not escape from the rotor during the exhausting process (port 4). This exhaust gas recirculation is a unique aspect of this particular type of four-port cycle. There are other configurations in which it does not occur.[3] It is not known at this point whether it represents an advantage or disadvantage in terms of combustor design and/or pollution control.

#### Steady-State Performance

Before discussing dynamic results, it is worthwhile to briefly review the steady-state wave rotor characteristics. Doing so provides a reference against which to measure the deviations from normal operation exhibited by the dynamic simulations. If perfect gas behavior and constant dynamic viscosity are assumed, and if the weak Reynolds number dependency [note the exponent in the momentum source term of Eq. (4)] is neglected, then the steady-state performance of a wave rotor topping cycle can be described in terms of $\gamma$, and the following three dimensionless variables:

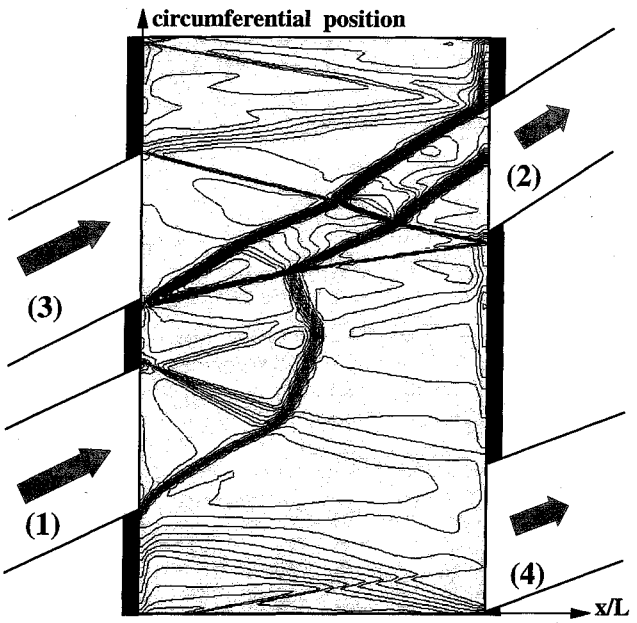


**Fig. 2 Design point density contours.**

$$\omega_c = \omega\sqrt{A_{in}/R_gT'_{in}g_c}$$
$$\dot{m}_c = (\dot{m}_{in}/A_{in}P'_{in})\sqrt{R_gT'_{in}/g_c} \tag{16}$$
$$Q_c = \frac{Q}{A_{in}P'_{in}\sqrt{R_gT'_{in}g_c}}$$

The first two variables are essentially corrected speed and corrected mass flow rate. The last variable, corrected heat addition, is not normally used to describe turbomachinery performance (although it could be), because the compressor and turbine components are usually considered separately. This is not possible on the wave rotor, however, since compression and expansion occur on the same device and are highly coupled. Given $\gamma$ and the variables of Eq. (16), any other variable of interest can be represented as a dimensionless function of these four. For instance, from a steady-state topping cycle operability point of view, one would be interested in knowing the stagnation pressure and temperature ratios across the entire wave rotor as functions of these variables. Referring to Fig. 1, this would be $P_4/P_1$ and $T_4^0/T_1^0$. If, as is done in the model, $\gamma$ is assumed constant, then one independent variable would be eliminated. A multidimensional map would still be required, however, which is difficult to envision. It has been observed in cycle deck studies of the type of wave rotor topping cycle under consideration here[3] that, for small turboshaft engines, optimal performance is found along a constant corrected speed line for most of the operating range (neglecting startup and idle modes). Furthermore, although the effect that off-design flow turning has on performance can be large,[7] the amount of work done on the gas is relatively small compared to the heat addition. If this shaft work is neglected, then the temperature ratio may be obtained from the corrected mass flow rate and heat addition as

$$T_4^0/T_1^0 = 1 + [(\gamma - 1)/\gamma](Q_c/\dot{m}_c) \tag{17}$$

Thus, the desired wave rotor performance may be expressed on a single plot that shows overall pressure ratio as a function of corrected mass flow rate for different families of corrected heat addition. Such a map is shown in Fig. 3 for the particular

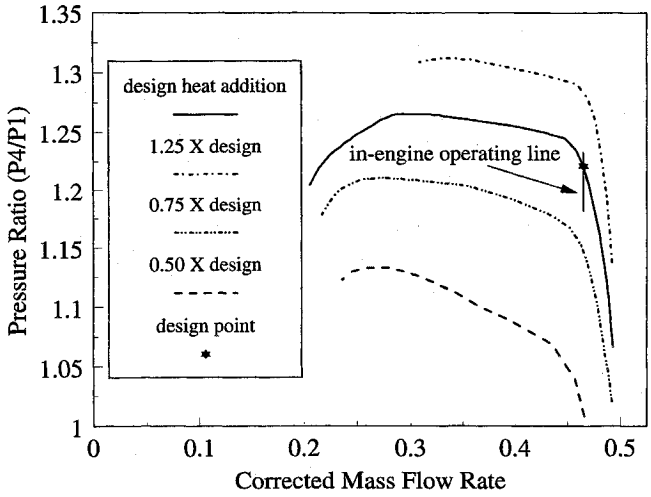


**Fig. 3 Constant speed, steady-state performance map.**

wave rotor described earlier. This map was generated using the single-passage, steady-state model described in Refs. 1 and 5–7, and verified at several points using the present model. Also shown in the figure is the design operating point, and a line representing the locus of normal, steady-state operating points, in an engine environment[3] (i.e., with an upstream compressor and downstream turbine) for a range of throttle positions.

## Dynamic Results

The arrangement of the transient simulation is shown in block schematic form in Fig. 4. The valve attached to the exhaust port (4) is modeled similarly to the combustor, though without heat addition, and is described fully in Ref. 12. It is assumed to exhaust to standard atmospheric conditions. The wave rotor inlet is assumed to be at conditions representative of the hypothetical upstream compressor exit. For the results to be presented, these conditions were held constant at the reference state shown in Table 1. In this numerical test cell environment the exhaust valve area and heat addition rate are inputs and can be independently altered. Any other wave rotor variable of interest is an output and can be monitored. In addition, the combustor, valve, and center cavity volumes can be altered to isolate their effect on transient phenomena.

### Transient Responses to Step Inputs

The computed wave rotor response to a step change in heat addition is shown in Figs. 5 and 6. The model ran for 20 ms of simulation time at the design point. At that time the heat

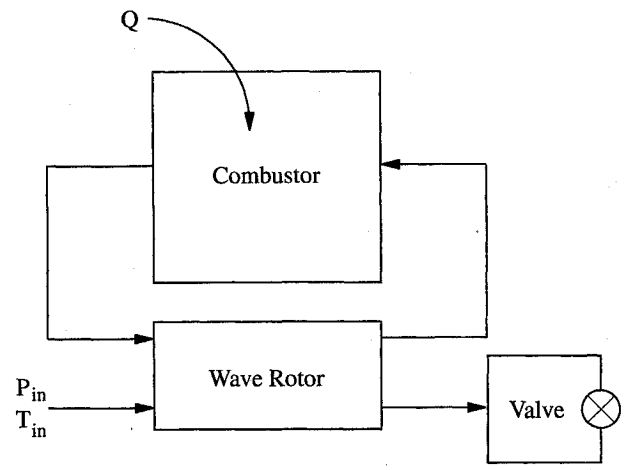


**Fig. 4 Block schematic of simulation.**

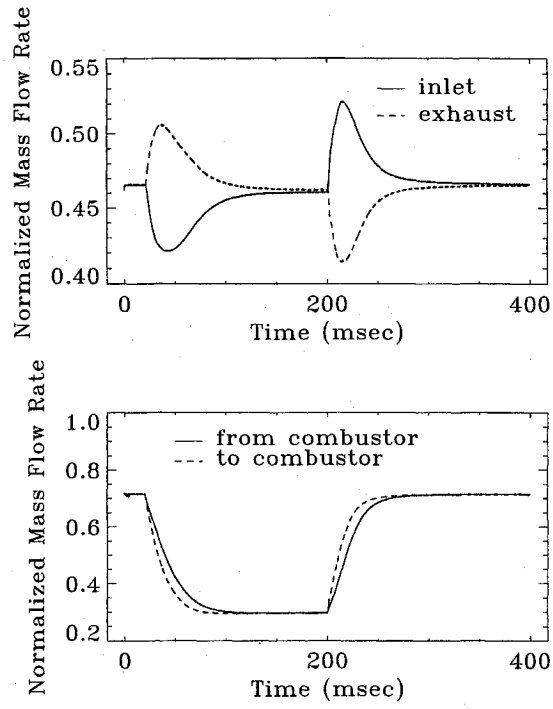


**Fig. 5 Step heat addition rate change transient port mass flow rates.**

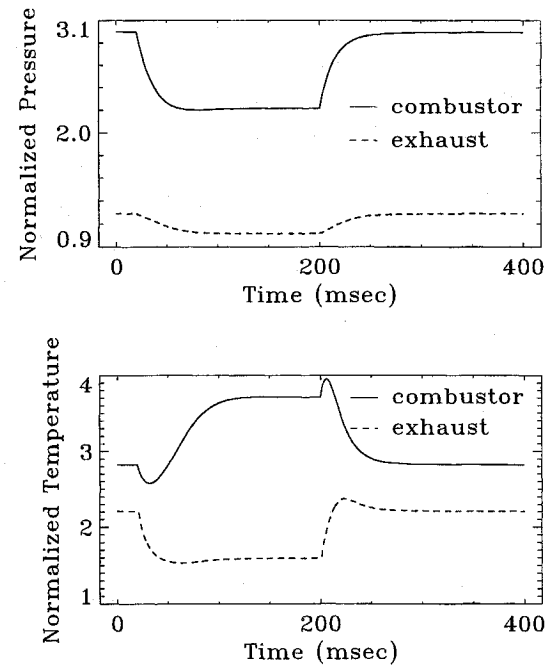


**Fig. 6 Step heat addition rate change transient pressures and temperatures.**

addition rate was abruptly cut to half of the design value. At 200 ms of simulation time the heat addition rate was abruptly raised back to the design value and held there for the remainder of the 400-ms simulation. The ratios of passage volume to the center cavity, combustor, and valve volumes in Eqs. (11), (12), and (23) were 0.0093, 0.0037, and 0.018, respectively. The mass flow rates in each of the ports are shown in Fig. 5. These, and all subsequently plotted mass flow rates, have been normalized by the inlet port (Fig. 1) area, stagnation pressure, and stagnation temperature as in Eq. (16). For the inlet only, this is the corrected flow and corresponds to the $x$ axis of Fig. 3. Figure 6 shows nondimensional stagnation pressures and

temperatures in the combustor and exhaust port. Since the inlet stagnation state has been used to nondimensionalize, the exhaust pressure in this figure corresponds to the $y$ axis of Fig. 3. The simulation data were output at a time interval of 0.011 ms (every six nondimensional time steps), then low-pass filtered using a cutoff frequency of 1600 Hz to remove the high-frequency oscillations that occur because of the finite passage opening time. These oscillations, though small, tend to mask the other wave rotor dynamics. For example, the peak-to-peak mass flow oscillations of the simulation shown in Fig. 5 were approximately 2.2% of the design point inlet mass flow rate. For reference, a single passage of the wave rotor completes an entire wave cycle (Fig. 2) at the rate of 560 Hz. The transient behavior seen in this simulation example is almost entirely because of the volume dynamics associated with the combustor, center cavity, and valve. That is to say that the wave rotor is essentially operating in steady-state even though the inlet and exhaust mass flow rates do not match one another, nor do the flow rates to and from the combustor. This may be seen in Fig. 7 that shows the sum of the normalized mass flow rates to and from all of the ports as a function of time. The upper plot shows the entire simulation period, whereas the lower plot shows only the first 52 ms. If mass were being stored in the wave rotor (or center cavity), this sum would be large; however, it is seen that the sum never exceeds 0.02, whereas the difference between inlet and exhaust mass flow rates (Fig. 5) reaches values as high as 0.1. The relatively fast response of the wave rotor itself can be seen on the lower plot of Fig. 7 between 20–23 ms. The first minimum on this plot (between 20–20.5 ms) represents the readjustment time of the waves. The maximum that follows, of somewhat longer duration, represents the convection time for a particle passing through the rotor. The remaining transient response is because of the volume dynamics of the center cavity.

It is interesting to note that during this transient operation the combustor pressure (i.e., the compression portion of the cycle) decreases with decreasing inlet flow when the heat addition rate is reduced, and vice versa when the heat addition rate is increased. In a conventional gas-turbine engine, the initial transient behavior would be the opposite manner.

The wave rotor mass flow, pressure, and temperature response to a step change in the exhaust valve area are shown in Figs. 8 and 9. As in the previous simulation the model ran for 20 ms of simulation time at the design point. At that time the exhaust valve area was abruptly cut to 80% of the design value. At 200 ms of simulation time the valve area was abruptly increased back to the design value and held there for the remainder of the 400-ms simulation. The ratios of passage volume to the cavity, combustor, and valve volumes were the same as in the previously described simulation. Figure 10 shows the same type of mass flow summation as Fig. 7. Again it can be seen that the response of the wave rotor is very fast relative to the various volume dynamics. With regard to Fig. 3, it can be seen that both this and the previously presented

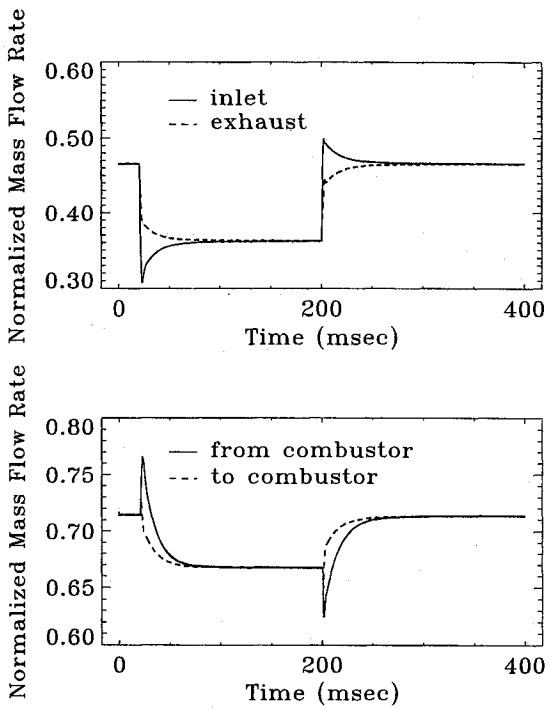


**Fig. 8 Step exhaust valve area change transient port mass flow rates.**

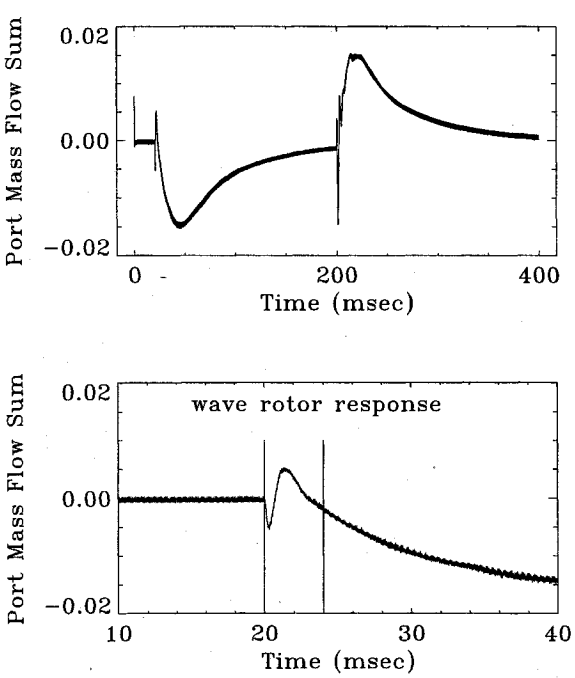


**Fig. 7 Step heat addition rate change transient port mass flow rate summation.**

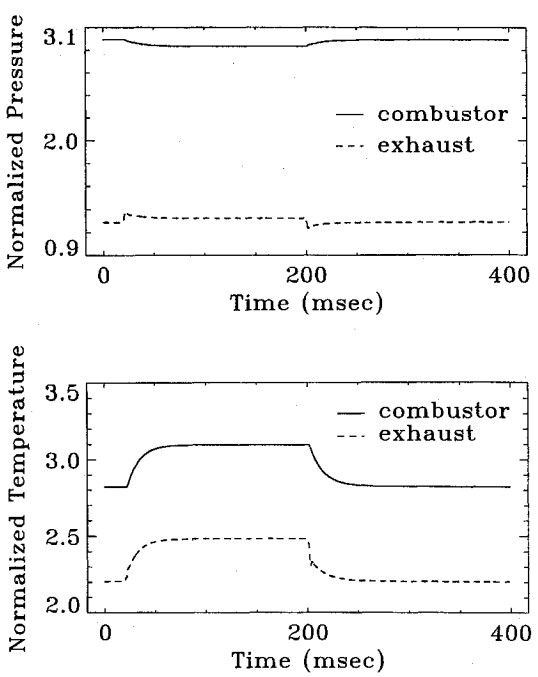


**Fig. 9 Step exhaust valve area change transient pressures and temperatures.**

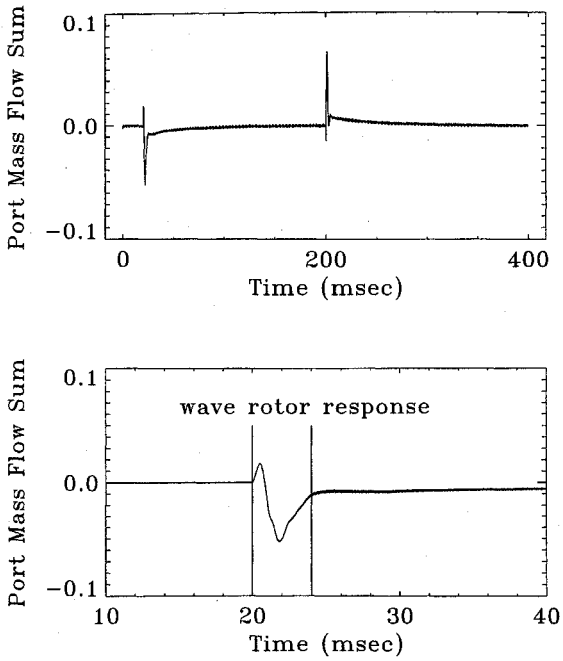


**Fig. 10 Step exhaust valve area change transient port mass flow summation.**

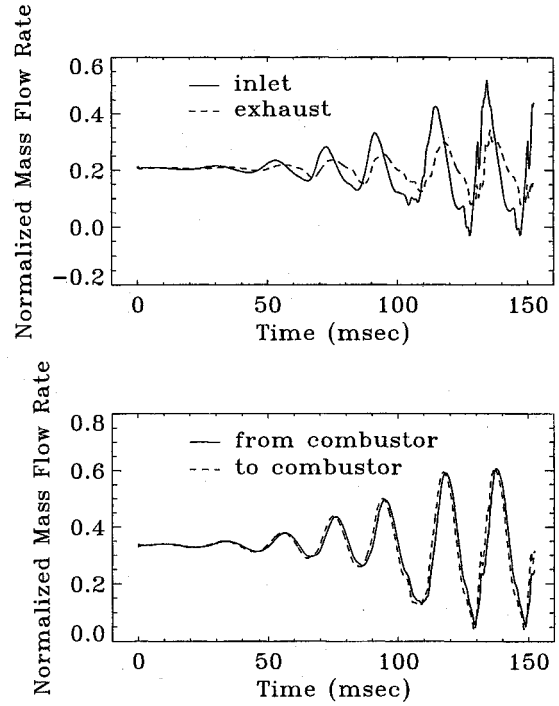


**Fig. 11 Unstable surge port mass flow rates.**

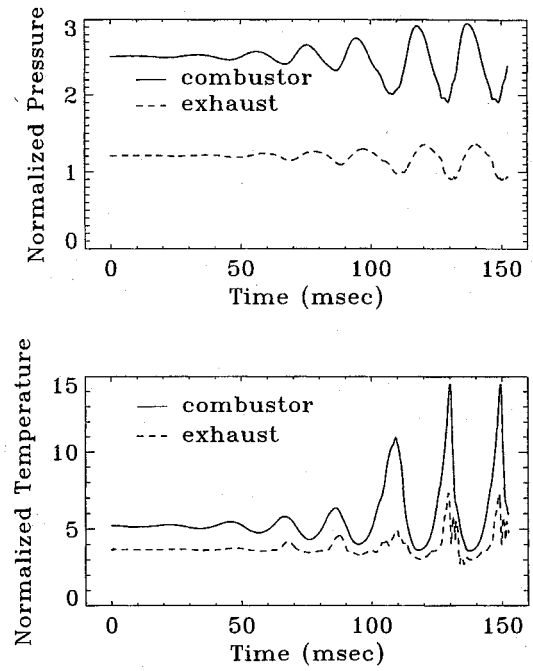


**Fig. 12 Unstable surge pressures and temperatures.**

transient represent situations in which the wave rotor is operating far from the normal range. It is encouraging from a modeling perspective that the simulation can calculate such severe transients. More importantly, however, it is encouraging that the wave rotor appears to be so robust.

### Instabilities

Although it is not yet possible to experimentally verify the results of the wave rotor model described earlier, it is at least possible to see if it follows expected dynamic trends. One such trend would be a phenomenon akin to surge which, with reference to Fig. 3, would occur when the wave rotor is operating somewhere on the far left side of the constant heat addition curves where the slopes of the performance curves are positive.[13] It should be pointed out that this region is far from the normal in-engine operating regime of the wave rotor shown by the vertical line in Fig. 3 (although it is conceivable that such a point may be reached during a startup or idle transient). Furthermore, steady-state results indicate that long before it could reach this point the combustor temperatures would become unacceptably high (i.e., five times the inlet temperature). Nevertheless, attempting to operate the model here provides a good test for the numerics. Figures 11 and 12 show a time history of the port normalized mass flows, and plenum pressures and temperatures during a simulation that began at the design speed and heat addition rate, but with the exhaust valve area reduced to 58% of the design point value. Note that the vertical axis of the upper plot in Fig. 11 corresponds to the horizontal axis of Fig. 3, so that by noting the flow rate at the beginning of the surge simulation it is possible to see where the wave rotor was operating on the steady-state map just prior to the onset of instability. The valve position at which this instability begins is dependent on the combustor and valve (and possibly center cavity) volumes. It was found that the simulation was stable at this operating point for the passage-to-volume ratios used in the previous simulations. The exact relationship between volume sizes and the onset of this instability has not been fully explored; however, it was found that decreasing the combustor volume and increasing the valve volume both appear to shift the point of instability further to the right of Fig. 3 (i.e., larger exhaust valve openings). Thus, the data for Figs. 11 and 12 were obtained by first running the simulation to steady state using the original center cavity, combustor, and valve passage to volume ratios of 0.0093, 0.0037, and 0.018, respectively. The passage-to-volume ratios of the combustor and valve were then changed to 0.037 and 0.0062, respectively, and the simulation was restarted with initial conditions from the last time step of the stable simulation configuration. Figure 12 shows stagnation pressures and temperatures in the combustor and exhaust ports for this simulation. It can be seen that the combustor temperature periodically reaches very high values because of the periodically very low mass flow rates and constant heat addition rate. As such, it was necessary to substantially reduce the size of the time step in the computational scheme. It was found that a nondimensional

value of 0.0015 (compared to 0.006 used in the other simulations) maintained a stable computational scheme.

**Freewheeling Rotor**

The results shown thus far are for a wave rotor that runs at a constant speed and is driven by some external source. It is possible, however, for the wave rotor to be self-driven or freewheeling.[14] If bearing drag, friction between the rotor and endwalls, and friction between the rotor and casing are neglected, then the only source of torque on the rotor arises from the flow turning required to bring flow onboard the rotor from the ducts. At the design point, the inlet ducts would be so angled such that this would presumably be zero. At any other operating point, however, the rotor will either accelerate or decelerate until the net torque is zero. In this mode of operation the corrected speed becomes a dependent variable and Eq. (17) becomes absolutely valid. It is noted that in steady-state operation there is no guarantee that the speed that the rotor settles out to at any operating point (other than the design point) is optimal as far as the timing of the internal wave processes. Figure 13 shows the steady-state performance map for the freewheeling version of the same wave rotor used in the fixed speed examples. Note that the design points of the two rotors are the same. Compared with Fig. 3, this map shows regions of only slightly positive slope at low mass flow rates. This may indicate more stable operation than the fixed speed configuration in this regime.

Figure 14 shows the wave rotor response to a step 50% reduction in the heat addition rate initiated 2.0 ms after the simulation began. The time scale of this simulation is very long in comparison to the others, which have been shown previously. This is because of the relatively slow rotor inertial dynamics that are made even slower by the fact that the flow turning process generates fairly low torque (unlike conventional turbomachinery in which torque is the primary means of work transfer). To produce the data for Fig. 14 without using excessive computing resources, a very crude computational spacing of $\Delta x = 0.1$ was used with a corresponding time step of $\Delta t = 0.03$. Furthermore, the data were output only every 0.36 ms. No systematic study has been performed to date on the model to determine the best grid resolution for simulation purposes; however, it is believed that these values of the time step and spacing are sufficient to reasonably demonstrate the rotordynamic phenomenon of interest here. The inertia of the rotor was estimated using steel with a density of 7860 kg/m$^3$ and assuming that the only contributing mass was that of the inner and outer cylinders of the rotor. These were taken to be 0.76 cm in thickness. The figure shows plots of the inlet corrected flow rate, nondimensional combustor pressure, rotor corrected speed, and the summation over all of the computational cells of the rates of change in nondimensional wall temperature. This last plot is included as a very crude measure of the predicted time scale of the heat transfer effects in the wave rotor. The fact that a relatively large gradient still exists at the end of the simulation indicates the scale is considerably longer than even the rotor dynamic time scale, which is itself two orders of magnitude larger than the volume dynamic time scales, and three to four orders larger than the gasdynamic time scales.

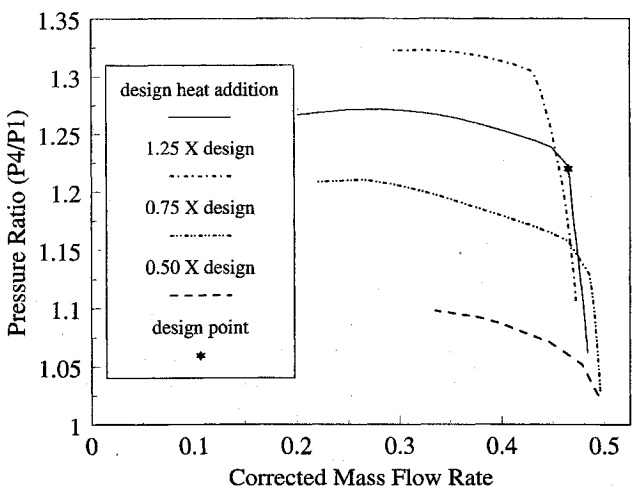


**Fig. 13 Freewheeling, steady-state performance map.**

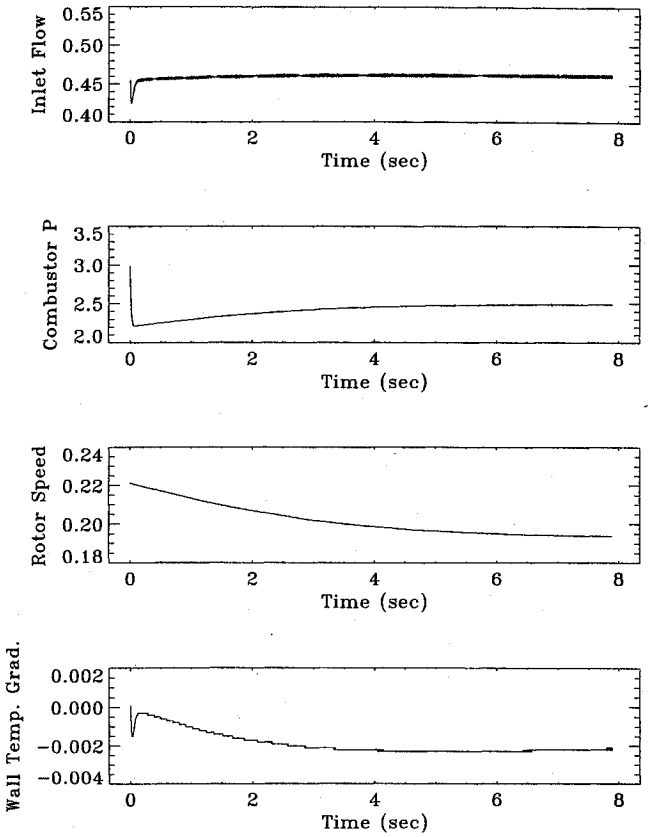


**Fig. 14 Freewheeling wave rotor: step heat addition rate change transient.**

It can be seen in Fig. 14 that the wave rotor performance is fairly insensitive to changes in rotational speed. Thus, although the rotor speed does not reach steady state until 8 s after the step reduction in heat addition rate, the combustor pressure and inlet flow have reached nearly steady-state values in the same approximately 50-ms time frame as the previous fixed speed transient examples. This is in contrast to a conventional turbomachinery core that would require time scales on the order of seconds to complete the same transient.

## Concluding Remarks

A numerical model has been described that is capable of computing both steady-state and transient flowfields in a wave rotor. Since it is a one-dimensional model it is relatively fast. The grid resolution used for the constant speed simulations required approximately 143 s of CPU time for each millisecond of simulated time on a SunSPARC 10 workstation. The freewheeling simulation ran at approximately 25 times that rate because of a five-times increase in the time step size and a corresponding five-times reduction in the number of computational cells. Although no experimental transient wave rotor data are available with which to compare, the model predicts results that qualitatively meet expectations, including the onset of instabilities in the far off-design operating regime.

The preliminary results presented in this article suggest that the wave rotor response to transient input is an order of magnitude faster than the external volume dynamics and approxi-

mately three orders of magnitude faster than the freewheeling rotor dynamics. Furthermore, it appears that the wave rotor is stable over a wide range of transient operations.

Ultimately, the dynamic performance of the wave rotor topping cycle can only be properly assessed in an integrated engine simulation environment since the behavior of the surrounding turbomachinery will have a large influence on the wave rotor. This is the intended direction of future research in the type of one-dimensional modeling presented in this article.

## References

[1]Paxson, D. E., "A Comparison Between Numerically Modelled and Experimentally Measured Loss Mechanisms in Wave Rotors," *Journal of Propulsion and Power*, Vol. 11, No. 5, 1995, pp. 908–914.

[2]Wilson, J., and Paxson, D. E., "Jet Engine Perfomance Enhancement Through the Use of a Wave-Rotor Topping Cycle," NASA TM 4486, Oct. 1993.

[3]Welch, G. E., Jones, S. M., and Paxson, D. E., "Wave Rotor Enhanced Gas-Turbine Engines," AIAA Paper 95-2799, July 1995.

[4]Wilson, J., and Paxson, D. E., "Optimization of Wave Rotors for Use as Gas Turbine Engine Topping Cycles," Society of Automotive Engineers Paper 951411, May 1995.

[5]Paxson, D. E., "A General Numerical Model for Wave Rotor Analysis," NASA TM 105740, July 1992.

[6]Paxson, D. E., "An Improved Numerical Model for Wave Rotor Design and Analysis," AIAA Paper 93-0482, Jan. 1993.

[7]Paxson, D. E., and Wilson, J., "Recent Improvements to and Validation of the One Dimensional NASA Wave Rotor Model," NASA TM 106913, May 1995.

[8]Holman, J. P., *Heat Transfer*, 5th ed., McGraw–Hill, New York, 1981.

[9]Egli, A., "The Leakage of Steam Through Labyrinth Seals," *Transactions of the American Society of Mechanical Engineers*, Vol. 57, 1935, pp. 115–122.

[10]Roe, P. L., "Characteristic Based Schemes for the Euler Equations," *Annual Review of Fluid Mechanics*, Vol. 18, 1986, pp. 337–365.

[11]Kays, W. M., and Crawford, M. E., *Convective Heat and Mass Transfer*, McGraw–Hill, New York, 1980.

[12]Paxson, D. E., "A Numerical Model for Dynamic Wave Rotor Analysis," NASA TM 106997, July 1995.

[13]Greitzer, E. M., "The Stability of Pumping Systems," *Journal of Fluids Engineering*, Vol. 103, June 1981, pp. 193–242.

[14]Zehnder, G., Mayer, A., and Matthews, L., "The Free Running Comprex®," Society of Automotive Engineers Paper 890452, Feb. 1989.